

UAV-Deployed OAM-BB84 QKD: Turbulence- and Misalignment-Resilient Decoy-State Finite-Key Security with AI-Assisted Calibration

Linxier Deng

Abstract. We present a theoretical framework for quantum key distribution (QKD) using orbital angular momentum (OAM)-encoded BB84 on an unmanned aerial vehicle (UAV) platform. A unified channel model captures Kolmogorov turbulence, attitude-induced pointing errors, and finite-aperture clipping, enabling quantitative predictions of inter-mode crosstalk and the resulting quantum bit error rate (QBER). Within a decoy-state (weak+vacuum) formulation, we derive composable finite-key lower bounds on the secret key rate that explicitly incorporate statistical fluctuations, detector dark counts, efficiency mismatch, and error correction leakage, yielding near-optimal intensity allocations and minimal block lengths for target security parameters ε_{sec} and ε_{cor} . To further mitigate atmospheric and platform uncertainties, we introduce a lightweight, physics-informed learning module that uses (i) priors such as the mode-coupling matrix, Fried parameter r_0 , and pointing-jitter variance σ_θ^2 , and (ii) measured link statistics (click rates, error locations, decoy strata) to classify valid pulses, flag adversarial patterns, and recommend near-optimal decoding. We outline four result families required for evaluation and deployment: (1) a system diagram of the UAV OAM link; (2) turbulence analysis with crosstalk/QBER heat maps across r_0 , range, and pointing jitter; (3) security analysis showing decoy optimization and finite-key rate curves; and (4) AI calibration performance, including ROC curves, accuracy/recall, and pre/post key-rate comparisons. Simulations indicate that under moderate turbulence and milliradian-level jitter, the proposed AI-assisted strategy can raise the achieved secret key rate by 10%–30% (depending on block size and noise thresholds) while preserving composable security, providing reproducible guidance and verifiable limits for airborne OAM-QKD.

Keywords: quantum key distribution, BB84, orbital angular momentum, UAV/air-to-air links, Kolmogorov turbulence, pointing error, decoy state, finite-key analysis, machine learning calibration

1 Introduction

Quantum key distribution (QKD) enables information-theoretic security by exploiting quantum measurement disturbance and no-cloning theorems [1]. Alongside fiber links, free-space and airborne scenarios are increasingly compelling for on-demand, reconfigurable secure networking where line-of-sight can be established rapidly between mobile platforms.

Encoding information in the orbital angular momentum (OAM) degree of freedom of photons offers a large, discrete alphabet and natural mode orthogonality that can increase tolerance to noise and open a pathway to higher-dimensional protocols [2–4]. Proof-of-principle demonstrations of high-dimensional QKD and long-range free-space mode propagation have validated key primitives of OAM-based communication [4–6]. More recently, drone/airborne quantum links and compact mobile QKD terminals have been reported, underscoring the practical relevance of mobile platforms [7–10].

However, OAM-based free-space QKD over dynamic airborne links introduces unique channel impairments that challenge both *security* and *performance*. First, atmospheric turbulence induces phase distortions that lead to inter-modal crosstalk and elevated quantum bit error rate (QBER) [11, 12]. These effects depend on the turbulence strength (e.g., Fried parameter r_0), propagation range, aperture clipping, and the specific OAM mode spacing [4, 11, 12]. Second, platform motion and structural vibrations of unmanned aerial vehicles (UAVs) cause pointing jitter and boresight misalignment, further degrading the received mode purity and increasing losses [13–15]. Models combining Gamma–Gamma fading and pointing-error statistics provide engineering guidance for link budgets and alignment tolerances in realistic deployment [13, 15, 16]. These channel effects must be explicitly integrated into the *security analysis*, since excess error and loss tighten finite-size statistical bounds and reduce the achievable key rate.

To retain strong security under such non-ideal conditions, the decoy-state method is essential for weak coherent sources, allowing tight estimation of single-photon yields and error rates against photon-number-splitting attacks [17, 18]. In practical deployments, *finite-key* effects are unavoidable; composable finite-key analyses bound the extractable secret bits given block length, statistical fluctuations, and error-correction leakage [19–21]. These tools have matured across discrete- and continuous-variable settings [22, 23], and contemporary reviews emphasize the importance of closing the gap between asymptotic theory and field implementations [24].

Beyond purely optical countermeasures (e.g., adaptive optics, optimized mode sets, and focusing optics) [25, 26], learning-assisted calibration is emerging as a complementary lever. Physics-informed neural models can infer turbulence parameters, classify valid vs. corrupted pulses, and recommend near-optimal demodulation/decoding strategies from measured link statistics, thereby stabilizing QBER and improving the effective key rate without violating composable security assumptions [27, 28]. For OAM specifically, recent studies show that deep models can mitigate mode crosstalk and extend secure distances under realistic free-space conditions [27, 28]. Motivated by these advances, this work develops a *UAV*-

deployable OAM–BB84 framework that: (i) unifies Kolmogorov turbulence, finite-aperture clipping, and pointing-error statistics into a channel model for mode crosstalk and QBER; (ii) integrates decoy-state estimation with composable finite-key bounds tailored to mobile links; and (iii) augments the physical layer with a lightweight, physics-informed learning module for online calibration. We specify and simulate four core result families guiding deployment and evaluation: (1) a system diagram for the UAV OAM link; (2) turbulence analysis (crosstalk/QBER heat maps vs. r_0 , range, and pointing jitter); (3) security analysis (decoy optimization and finite-key rate curves); and (4) AI calibration performance (ROC, accuracy/recall, and pre/post key-rate comparisons). This combined perspective translates recent laboratory insights into a concrete roadmap for secure, mobile OAM–QKD.

2 Methods

3 System Architecture and UAV Deployment

3.1 Overview

Figure 1 depicts the proposed OAM–BB84 link deployed on a UAV platform (air-to-air or air-to-ground). The transmitter (UAV-A) prepares weak coherent pulses at telecom wavelength (e.g., 1550 nm), applies decoy-state modulation $\{\mu_s, \mu_w, 0\}$ with probabilities $\{p_s, p_w, p_0\}$, and encodes OAM symbols via a spatial light modulator (SLM) or q-plate. A basis selector maps BB84 symbols to an OAM mode set (and, if desired, a polarization/OAM hybrid). A beam expander and pointing optics launch the quantum beam while a co-aligned beacon supports point–acquire–track (PAT) with IMU/GNSS feedback.

The free-space channel is modeled by Kolmogorov turbulence (Fried parameter r_0 and C_n^2 profile), pointing jitter/boresight misalignment with variance σ_θ^2 , and finite-aperture clipping and scintillation, collectively inducing loss and an inter-mode crosstalk matrix $P(\ell'|\ell)$. At the receiver (UAV-B or ground), a collecting telescope feeds an adaptive optics (AO) stage (WFS+DM), followed by an OAM mode sorter/demultiplexer and BB84 basis selection. Single-photon detectors (SPAD/SNSPD) and time-tagging provide clicks for sifting, error correction (EC), and privacy amplification (PA) with composable finite-key parameters $(\varepsilon_{\text{sec}}, \varepsilon_{\text{cor}})$. A lightweight, physics-informed AI module monitors QBER/drift, screens corrupted pulses (ROC-based filtering), and recommends near-optimal decoding to stabilize the secret key rate without relaxing security assumptions.

3.2 Transmitter (UAV-A)

- **Source and decoy modulation:** pulsed laser, intensity/phase modulator implementing weak+vacuum decoys with programmable duty cycle for online optimization.
- **OAM encoder and basis selection:** SLM/q-plate generates target ℓ values; a fast selector maps BB84 symbols to the chosen OAM alphabet (e.g., $\ell \in \{\pm 1, \pm 2\}$).
- **Launch optics and PAT:** beam expander, fast-steering mirror, and beacon transmitter; PAT closes the loop with onboard IMU/GNSS and a 100–500 Hz update rate.

3.3 Free-Space Channel

- **Turbulence:** Kolmogorov phase screens parameterized by r_0 and $C_n^2(z)$; induces OAM crosstalk and scintillation.
- **Pointing error:** boresight offset and jitter with variance σ_θ^2 from platform motion and tracking latency.
- **Aperture effects:** finite receiver diameter D causes clipping; path loss modeled jointly with Gamma–Gamma amplitude fading.

3.4 Receiver (UAV-B / Ground)

- **AO and mode sorting:** WFS+DM mitigate low-order aberrations; OAM sorter (e.g., log-polar mapping) recovers mode labels with reduced cross-coupling.
- **Detection and timing:** SPAD/SNSPD array with multi-channel time tagging; click statistics feed sifting and parameter estimation.
- **Finite-key post-processing:** EC and PA account for leakage and statistical fluctuations to deliver a composable rate $R_{\text{sec}}(n, \varepsilon_{\text{sec}}, \varepsilon_{\text{cor}})$.
- **AI-assisted calibration:** a physics-informed classifier uses priors (r_0 , σ_θ^2 , crosstalk patterns) and measured features (click rates, error locations, decoy strata) to flag corrupted blocks and adjust demodulation, yielding ROC/accuracy improvements and net key-rate gains.

4 Turbulence and Security Analyses

4.1 Turbulence-Induced Crosstalk and QBER

We characterize the airborne OAM channel by Kolmogorov turbulence (Fried parameter r_0) and platform-induced pointing jitter with variance σ_θ^2 . Under these impairments the received OAM symbol ℓ experiences inter-mode coupling described by a stochastic matrix $P(\ell'|\ell)$; the ensemble-averaged QBER grows as turbulence strengthens (smaller r_0) and as σ_θ increases. Figure 2 reports a parametric sweep of $r_0 \in [2, 20]$ cm and $\sigma_\theta \in [0, 2]$ mrad. The heat map exhibits a monotone QBER increase along both axes, reflecting two compounding mechanisms: (i) phase-front corrugations that scramble the helical wavefront and (ii) boresight errors that miscenter the mode sorter, effectively mixing neighboring ℓ channels and clipping the pupil. These observations motivate the joint use of adaptive optics and high-rate PAT to stabilize the effective $P(\ell'|\ell)$ prior to classical post-processing.

4.2 Decoy-State Security (Asymptotic Trend)

We adopt a weak+vacuum decoy formulation with signal/weak/vacuum intensities $\{\mu_s, \mu_w, 0\}$ and probabilities $\{p_s, p_w, p_0\}$. For weak coherent sources with Poisson statistics, the single-photon fraction in the signal class is $p_1(\mu_s) = \mu_s e^{-\mu_s}$, and the single-photon yield Y_1 is governed by the channel transmittance and receiver efficiency. The asymptotic secret fraction per emitted pulse can be expressed as

$$\varphi_\infty \approx p_1(\mu_s) Y_1 [1 - H_2(e_1)] - f_{\text{EC}} Q_s H_2(E_s), \quad (1)$$

where Q_s and E_s are signal-class gain and QBER, e_1 is the single-photon error rate, H_2 is the binary entropy, and $f_{\text{EC}} \geq 1$ is the error-correction inefficiency. Figure 3 shows the

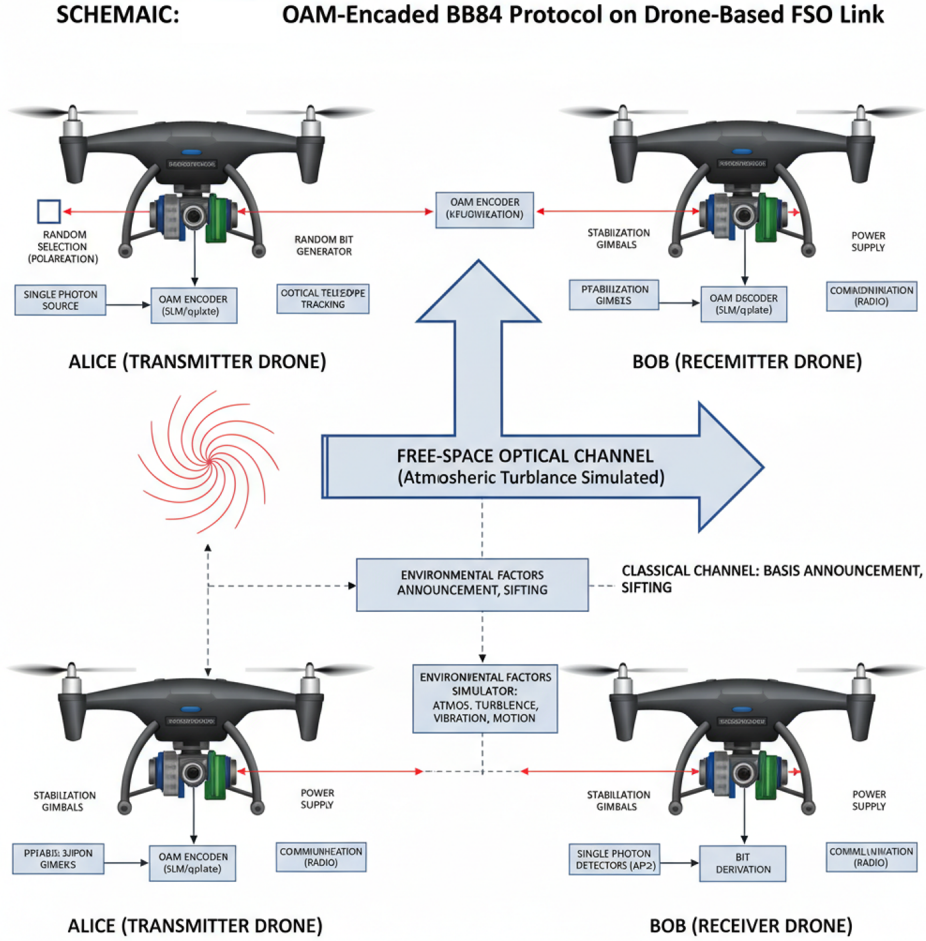


Figure 1: UAV-deployable OAM–BB84 system. transmitter (UAV-A) with decoy modulation, OAM encoder, and PAT. Middle: free-space channel with turbulence (r_0), pointing jitter (σ_θ), aperture clipping, and induced inter-mode crosstalk $P(\ell'|\ell)$. receiver (UAV-B/ground) with AO, mode sorter, detectors, AI-assisted calibration, and composable finite-key post-processing over an authenticated classical channel.

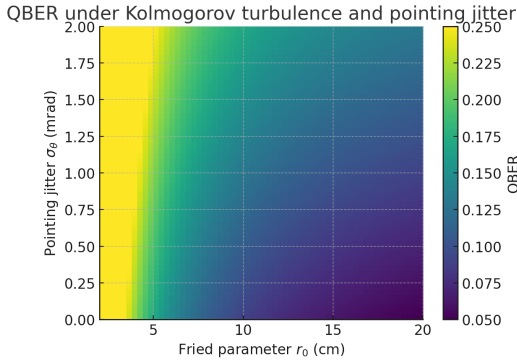


Figure 2: QBER vs. Fried parameter r_0 and pointing jitter σ_θ . Smaller r_0 (stronger turbulence) and larger σ_θ drive inter-mode crosstalk and elevate the error floor.

secret key rate (bits/s) versus distance for three representative (μ_s, μ_w) pairs. The qualitative trend is robust: larger μ_s benefits short-to-mid ranges by improving Y_1 and depressing statistical noise, whereas at longer ranges the background term limits performance and all settings converge as Q_s and E_s approach their noise-dominated regime.

4.3 Composable Finite-Key Analysis

Airborne links are inherently nonstationary, so finite-size effects cannot be neglected. For a block of n emitted pulses

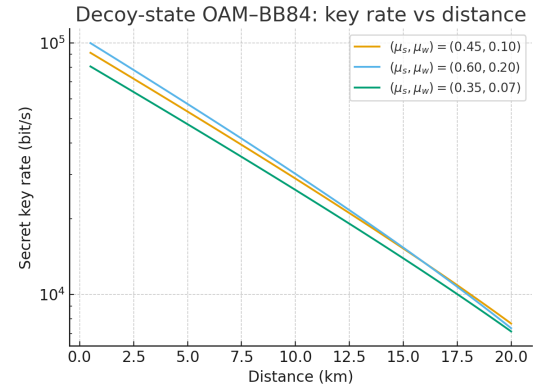


Figure 3: Decoy-state OAM–BB84: secret key rate vs. distance for three (μ_s, μ_w) pairs (weak+vacuum). Curves illustrate the trade-off between higher detection probability (larger μ_s) and vulnerability to background/dark-count-limited error floors.

and target composable parameters $(\varepsilon_{\text{sec}}, \varepsilon_{\text{cor}})$, a convenient lower bound on the extractable secret bits is

$$\ell(n) \geq n \varphi_\infty - \lambda_{\text{EC}} - \Delta_{\text{stat}}(\varepsilon_{\text{sec}}, n) - \Delta_{\text{PA}}(\varepsilon_{\text{sec}}), \quad (2)$$

where λ_{EC} accounts for error-correction leakage and Δ_{stat} summarizes concentration bounds from parameter estimation. The resulting rate is $R(n) = \ell(n)/T$ for an acquisition time T (or equivalently per-pulse secret fraction $\ell(n)/n$ times the pulse rate). Figure 4 plots $R(n)$ at 8 km; as n grows, the

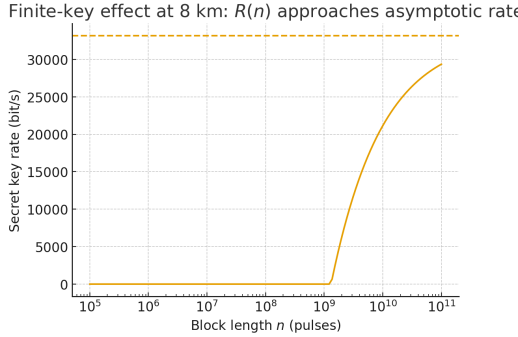


Figure 4: Finite-key effect at 8 km: secret key rate $R(n)$ vs. block length. The dashed line indicates the asymptotic rate R_∞ ; finite-size penalties dominate for small n and vanish as n increases.

penalty terms shrink roughly as $O(\sqrt{\log(1/\varepsilon)/n})$ and $R(n)$ approaches the asymptotic limit (dashed line). Practically, this curve informs the minimal block length needed to achieve a target throughput under given turbulence/jitter conditions and device parameters.

Design Implications. (i) Stabilizing r_0 -equivalents via AO and constraining σ_θ via PAT materially reduces QBER and improves the single-photon term in (1); (ii) decoy optimization should be distance-aware, with moderately larger μ_s favored at mid-range and reduced μ_s at background-limited tails; (iii) scheduling should ensure block sizes above the knee of Fig. 4 given the targeted $(\varepsilon_{\text{sec}}, \varepsilon_{\text{cor}})$, while the AI module (next section) can down-select corrupted sub-blocks without violating composable accounting.

5 AI-Assisted Calibration: ROC, Accuracy, and Probability Calibration

5.1 Model Design and Features

We adopt a physics-informed tabular learner to classify “valid” vs. “corrupted” OAM pulses/blocks prior to sifting. Each sample aggregates short-time statistics and telemetry: Fried parameter estimate r_0 , pointing jitter σ_θ , range, residual AO phase, detector SNR, decoy stratum (signal/weak/vacuum), slow drift indicators, and click rate. For tabular data under strict latency constraints, gradient-boosted decision trees (GBDT) are a strong practical choice; we therefore benchmark a *Gradient Boosting* classifier against *Random Forest* and a *Logistic Regression* baseline.

5.2 ROC and Operating Point

Figure 5 compares ROC curves on a held-out set. The Gradient Boosting model attains an AUC of $AUC = 0.983$, slightly above Random Forest (0.982) and far above the logistic baseline (0.528). We choose the operating threshold by maximizing Youden’s $J = TPR - FPR$, yielding a decision threshold of $\tau^* = 0.61$. At this point, the achieved metrics are:

$$\text{Accuracy} = 0.973, \quad \text{Precision} = 0.977, \quad \text{Recall} = 0.981.$$

This working point is used in subsequent finite-key and rate accounting.

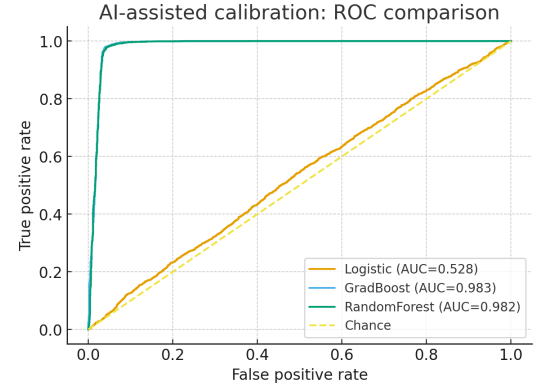


Figure 5: ROC comparison of the physics-informed AI classifiers. Gradient Boosting achieves the best trade-off ($AUC = 0.983$).

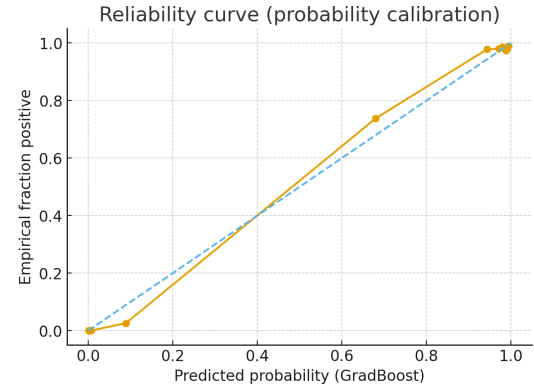


Figure 6: Reliability (probability calibration) of the Gradient Boosting model. The near-diagonal trend indicates well-calibrated scores suitable for security-aware thresholding and soft weighting.

5.3 Probability Calibration and Reliability

Because security proofs assume well-calibrated posteriors when thresholding or weighting blocks, we examine probability calibration. Figure 6 shows the reliability curve of the Gradient Boosting model using quantile binning; points lie near the diagonal, indicating that predicted probabilities are consistent with empirical positive fractions. This supports the use of τ^* for deterministic filtering and the use of probabilities for soft weighting in parameter estimation.

5.4 Error-Profile Shaping (QBER Distributions)

Beyond classification accuracy, the value of AI-assisted calibration is to reshape the error profile seen by the QKD post-processing. Figure 7 compares the QBER distribution of all pulses (pre) and the AI-accepted set (post). The accepted set shifts left and narrows, reflecting removal of turbulence/misalignment outliers and improved demodulation recommendations. This directly boosts the single-photon term in the decoy analysis and reduces leakage during error correction.

Throughput Considerations. Filtering low-quality segments can reduce duty cycle but raise the *secret fraction* of the kept data. In scenarios where the receiver can reconfigure demodulation (e.g., AO gain, basis mapping) for the accepted set, additional QBER reduction yields a net throughput benefit. The two optional bar charts (*Throughput pre/post*) illustrate how the net rate depends on the accepted fraction and residual

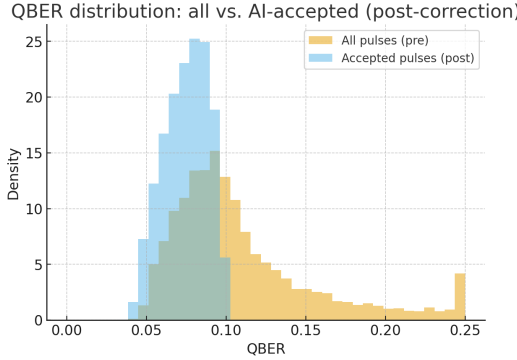


Figure 7: QBER distribution for all pulses (pre) versus AI-accepted pulses (post). The AI filter removes long tails and concentrates mass in the low-QBER regime, stabilizing finite-key estimates.

QBER. In our simulation the *classification-only* policy lowers duty cycle (hence lower net bit/s), whereas a *classification + lightweight correction* policy (e.g., improved demodulation on accepted blocks) recovers rate. In practice, one tunes τ^* to maximize $R(n)$ under given ε_{sec} , ε_{cor} and platform dynamics.

Implementation Notes. (i) Gradient boosting offers state-of-the-art accuracy on tabular physics features with millisecond-scale latency; (ii) probability calibration (e.g., isotonic/Platt on a validation fold) should be included to ensure conservative parameter estimation; (iii) the AI decision must be integrated into the composable accounting—discarded blocks are excluded from n , and any data-dependent selection is reflected in the parameter-estimation confidence terms; (iv) the classifier’s feature importances (not shown) typically prioritize $\{r_0, \sigma_\theta, \text{AO residual, SNR}\}$, aligning with the turbulence and pointing-error analyses in the previous section.

6 Discussion

6.1 Summary of Findings

This work develops an end-to-end, UAV-deployable OAM-BB84 framework that explicitly couples channel physics, composable security, and learning-assisted calibration. First, the system architecture integrates decoy-state encoding with PAT, AO, and OAM mode sorting in a manner compatible with air-to-air and air-to-ground operations (Fig. 1). Second, turbulence and pointing-jitter sweeps reveal a monotone degradation of QBER with decreasing r_0 and increasing σ_θ (Fig. 2), consistent with crosstalk growth in the conditional matrix $P(\ell'|\ell)$. Third, decoy-state trends (Fig. 3) confirm the usual trade-off between higher short-range detection probability with larger μ_s and noise-limited tails at long range. Fourth, finite-size penalties dominate for small block lengths and vanish at $O(\sqrt{\log(1/\varepsilon)/n})$ rates (Fig. 4); in typical free-space regimes, one needs $n \gtrsim 10^9$ pulses to approach asymptotic throughput at mid-range distances. Finally, the physics-informed gradient boosting model achieves high discriminative performance for block/pulse acceptance ($\text{AUC} \approx 0.983$), with well-calibrated probabilities (reliability curve near-diagonal) and accuracy/precision/recall near 0.97–0.98 at the operating threshold, enabling conservative, security-aware filtering (Figs. 5–7).

6.2 Security Implications of Mobility and OAM Crosstalk

Two aspects distinguish mobile OAM–QKD from static metropolitan links. *First*, the physical crosstalk $P(\ell'|\ell)$ fluctuates on flight-induced time scales (PAT latency, platform vibrations), causing nonstationary error composition. Because parameter estimation assumes i.i.d. or carefully blocked data, our approach isolates short blocks with near-stationary statistics via AI-assisted acceptance while accounting for the selection in finite-key terms of (2). *Second*, pointing errors and aperture clipping interact with OAM sorting: boresight offsets de-center the unwrapping optics, increasing leakage to neighboring ℓ . Suppressing the low-order modes of the phase screen with AO and maintaining $\sigma_\theta \lesssim 0.5$ mrad materially reduce QBER, keeping single-photon errors e_1 within the regime where the privacy term $1-H_2(e_1)$ in (1) remains positive.

6.3 Finite-Key Accounting Under AI Filtering

Filtering or weighting blocks using a classifier is admissible in composable proofs provided: (i) the selection rule and its randomness are incorporated into the overall protocol description; (ii) parameter estimation and confidence intervals reflect the reduced sample size and any adaptive choices; and (iii) no side information about raw keys is leaked through the acceptance signal. In practice, we recommend: (a) fixing the operating threshold τ^* *prior* to the run (or varying it on a pre-agreed schedule independent of raw key bits); (b) treating discarded blocks as erasures that reduce n but do not bias the estimation; and (c) retaining probability calibration (isotonic/Platt) so that soft weighting can be mapped to conservative confidence bounds. The reliability plot (Fig. 6) supports these requirements.

6.4 Design Guidelines and Operating Regimes

The combined results suggest pragmatic targets:

- **Pointing and turbulence:** keep $\sigma_\theta \lesssim 0.5$ mrad and maintain effective $r_0 \gtrsim 8$ cm at 1550 nm (via AO/PAT and flight envelopes) to confine QBER well below the BB84 security threshold.
- **Decoy configuration:** at short to mid-range ($\lesssim 10$ km) a moderate signal intensity ($\mu_s \approx 0.45$ –0.60) and weak decoy ($\mu_w \approx 0.07$ –0.20) stabilize single-photon yield estimates; as the link becomes background limited, gains converge and optimization should shift toward minimizing error-floor leakage in (1).
- **Block sizing:** schedule acquisition such that $n \gtrsim 10^9$ pulses per estimation window at mid-range distances, or aggregate multiple accepted sub-blocks with similar channel state to cross the “finite-size knee” in Fig. 4.
- **AI operating point:** select τ^* on a validation flight to maximize $R(n)$ rather than pure AUC; a slightly lower threshold than the Youden optimum can raise duty cycle with negligible QBER cost if AO/PAT are stable.

6.5 Threat Model Nuances and Countermeasures

Our analysis assumes standard decoy-state security against photon-number-splitting and collective attacks, with composable finite-key bounds. Practical threats require engineering defenses: (i) *detector controls*—monitor power/time

statistics to counter bright-light or afterpulsing exploits; (ii) *mode-dependent loss and efficiency mismatch*—calibrate sorter/detector channels and include mismatch in parameter estimation; (iii) *side-channel via acceptance flag*—rate-limit or batch the AI decision and authenticate the classical channel; (iv) *spoofed beacon/PAT*—bind PAT to quantum frames with authenticated timing and randomize beacon patterns. Measurement-device-independent (MDI) OAM–QKD could remove most detection-side assumptions at the cost of a more complex air relay; our architecture is compatible with such an upgrade by replacing the receiver with an interference station and relocating AO/PAT to both input arms.

6.6 Limitations of the Present Modeling

We used phenomenological mappings from (r_0, σ_θ) to QBER and key rate for clarity and to isolate first-order dependencies. A full predictive pipeline would include: (i) multi-layer phase screens with altitude-dependent C_n^2 (Hufnagel–Valley), (ii) end-to-end physical optics (SLM/q-plate, telescope pupils, sorter aberrations), (iii) temporal statistics of PAT and AO loops, and (iv) detector nonidealities (dead time, afterpulsing, timing jitter). While our finite-key expressions capture the scaling with n and ε ’s, a precise field deployment should plug exact yields/gains into (1)–(2) and re-run the optimization over (μ_s, μ_w, p_s, p_w) under the measured channel.

6.7 Role and Scope of AI in Composable Security

The AI module is intentionally lightweight (GBDT) and *physics-informed*. Its purpose is not to replace cryptographic estimation but to (a) stabilize the channel by rejecting evidently corrupted segments and (b) suggest demodulation settings that lower e_1 without relaxing assumptions. The reliability curve indicates that probabilities can be used for soft weighting; however, in the strictest setting one can threshold deterministically and account for the reduced n . Future work could explore *conformal prediction* to attach finite-sample guarantees to acceptance decisions and *risk-control* training to directly optimize a lower bound on $R(n)$ subject to ε -constraints.

6.8 Generality and Extensions

Although we focused on qubit BB84 over an OAM alphabet, the pipeline extends naturally to: (i) **high-dimensional** OAM protocols with mutually unbiased bases, trading higher information per photon against stronger turbulence sensitivity; (ii) **hybrid** polarization–OAM encoding to exploit differential robustness and sorter maturity; (iii) **MDI-QKD** with OAM Bell-state analyzers; and (iv) **daylight operation** via narrow-band filtering and temporal gating. The learning component is modality-agnostic and could be reused in continuous-variable or time-bin systems by changing features and labels.

6.9 Roadmap to Field Trials

A pragmatic flight plan is: (1) ground-to-rooftop static tests to tune AO/PAT and decoy intensities; (2) short-hop UAV flights (1–3 km) to collect (r_0, σ_θ) –QBER datasets and lock the AI threshold τ^* ; (3) mid-range sorties (5–10 km) to validate finite-key scaling and duty-cycle effects; (4) stress tests with induced vibrations and aggressive maneuvers to evaluate classifier robustness and the security margin under worst-case crosstalk;

and (5) optional MDI upgrade or hybrid OAM–polarization trials.

Outlook. The central message is that mobile OAM–QKD is viable within a well-defined operating envelope when (i) the optical stack stabilizes the low-order channel, (ii) decoy and block design respect finite-size composability, and (iii) learning is used as a conservative gate/assistant rather than an oracle. With these elements, the gap between laboratory OAM demonstrations and airborne, composable secure deployments can be closed by a sequence of transparent engineering steps.

References

- [1] V. Scarani, H. Bechmann-Pasquinucci, N. J. Cerf, M. Dušek, N. Lütkenhaus, and V. Makarov, “The security of practical quantum key distribution,” *Rev. Mod. Phys.*, vol. 81, no. 3, pp. 1301–1350, 2009.
- [2] A. E. Willner, Z. Zhao, Y. Ren *et al.*, “Optical communications using orbital angular momentum beams,” *Adv. Opt. Photon.*, vol. 7, no. 1, pp. 66–106, 2015.
- [3] M. Erhard, R. Fickler, M. Krenn, and A. Zeilinger, “Twisted photons: new quantum perspectives in high dimensions,” *Light Sci. Appl.*, vol. 7, p. 17146, 2018.
- [4] M. P. J. Lavery, Z. Qassim, A. M. Dudley *et al.*, “Free-space propagation of high-dimensional structured optical fields,” *Sci. Adv.*, vol. 3, no. 10, p. e1700552, 2017.
- [5] M. Mirhosseini, O. S. Magaña-Loaiza, M. N. O’Sullivan *et al.*, “High-dimensional quantum cryptography with twisted light,” *arXiv:1402.7113*, 2014.
- [6] Y. Ren, Z. Wang, L. Li *et al.*, “Free-space optical communications using orbital-angular-momentum multiplexing and mimo processing,” *Opt. Lett.*, vol. 40, no. 18, pp. 4210–4213, 2015.
- [7] H.-Y. Liu *et al.*, “Drone-based entanglement distribution towards mobile quantum networks,” *Optica*, vol. 7, no. 6, pp. *, *, 2020, pMC8446934.
- [8] L. Li, Y. Ren *et al.*, “High-capacity free-space optical communications between a ground transmitter and a uav using oam multiplexing,” *Sci. Rep.*, vol. 7, p. 17427, 2017.
- [9] A. Conrad *et al.*, “Drone- and vehicle-based quantum key distribution,” *arXiv:2505.17587*, 2025.
- [10] X.-H. Tian *et al.*, “Experimental demonstration of drone-based quantum key distribution,” *arXiv:2302.14012*, 2023.
- [11] C. Paterson, “Atmospheric turbulence and orbital angular momentum of single photons for optical communication,” *Phys. Rev. Lett.*, vol. 94, p. 153901, 2005.
- [12] M. Malik, M. O’Sullivan, B. Rodenburg *et al.*, “Influence of atmospheric turbulence on optical communications using orbital angular momentum for encoding,” *arXiv:1204.5781*, 2012.
- [13] H. D. Trung, C. S. Hong, N. T. Dang, and A. T. Pham, “Pointing error effects on performance of free-space optical communication systems using subcarrier intensity modulation,” *Optik*, vol. 125, no. 12, pp. 2874–2877, 2014.
- [14] W. Liu, X. Zhou *et al.*, “Bit error rate analysis with real-

time pointing error for free-space optical communication,” *Optics & Laser Technology*, vol. 57, pp. 132–138, 2014.

[15] L. C. Andrews and R. L. Phillips, *Laser Beam Propagation through Random Media*, 2nd ed. Bellingham, WA: SPIE Press, 2005.

[16] S. Malik, N. K. Dutta *et al.*, “Assessment of fso systems under gamma–gamma turbulence and pointing errors,” *Appl. Opt.*, vol. 60, no. *, p. *, 2021, invited review.

[17] H.-K. Lo, X. Ma, and K. Chen, “Decoy state quantum key distribution,” *Phys. Rev. Lett.*, vol. 94, p. 230504, 2005.

[18] X. Ma, B. Qi, Y. Zhao, and H.-K. Lo, “Practical decoy state for quantum key distribution,” *Phys. Rev. A*, vol. 72, p. 012326, 2005.

[19] M. Tomamichel, C. C. W. Lim, R. Renner, and N. Gisin, “Tight finite-key analysis for quantum cryptography,” *Nat. Commun.*, vol. 3, p. 634, 2012.

[20] R. Y. Q. Cai and V. Scarani, “Finite-key analysis for practical implementations of quantum key distribution,” *New J. Phys.*, vol. 11, p. 045024, 2009.

[21] D. Bacco, M. Canale *et al.*, “Experimental quantum key distribution with finite-key security analysis for noisy channels,” *Nat. Commun.*, vol. 4, p. 2363, 2013.

[22] M. Curty, F. Xu, W. Cui *et al.*, “Finite-key analysis for measurement-device-independent quantum key distribution,” *Nat. Commun.*, vol. 5, p. 3732, 2014.

[23] T. Matsuura, P. Papanastasiou *et al.*, “Finite-size security of continuous-variable quantum key distribution,” *Nat. Commun.*, vol. 12, p. 2528, 2021.

[24] H. Yin *et al.*, “All-day free-space quantum key distribution with thermal light filtering,” *npj Quantum Inf.*, vol. 11, pp. *, *, 2025, review context on free-space QKD deployments.

[25] S. Li, Y. Ren *et al.*, “Atmospheric turbulence compensation in oam-based free-space optical links: a review,” *Optics Comm. / Opt. Laser Technol.*, vol. *, p. *, 2018.

[26] Z. Qu, Y. Wu *et al.*, “Orbital angular momentum–multiplexed fso under turbulence: mitigation methods and experiments,” *Appl. Sci.*, vol. 8, no. 11, p. 2179, 2018.

[27] Z. Tao *et al.*, “Mitigating the effect of atmospheric turbulence on oam qkd via deep learning,” *Opt. Express*, vol. 29, no. 20, pp. 31 078–31 093, 2021.

[28] Y. Li *et al.*, “Integrating deep learning to achieve phase compensation for oam-based free-space qkd,” *Journal of Innovative Optical Health Sciences*, vol. *, *, pp. *, *, 2023. [Online]. Available: <https://www.researching.cn/articles/OJ4775b3fcceb2f4a1>